



Originally published as:

Thomas, P., Grott, M., Morschhauser, A., Vervelidou, F. (2018): Paleopole Reconstruction of Martian Magnetic Field Anomalies. - *Journal of Geophysical Research*, 123, 5, pp. 1140—1155.

DOI: <http://doi.org/10.1002/2017JE005511>

RESEARCH ARTICLE

10.1002/2017JE005511

Key Points:

- We use an Equivalent Source Dipole method to investigate six Martian crustal magnetic field anomalies
- Results indicate that at least one polar reversal event must have occurred on Mars
- Mars must have furthermore experienced significant true polar wander

Supporting Information:

- Supporting Information S1
- Figure S1
- Data Set S1
- Data Set S2
- Data Set S3
- Data Set S4
- Data Set S5
- Data Set S6
- Data Set S7
- Data Set S8
- Data Set S9
- Data Set S10
- Data Set S11
- Data Set S12
- Data Set S13
- Data Set S14
- Data Set S15
- Data Set S16
- Data Set S17
- Data Set S18
- Text S1

Correspondence to:

P. Thomas,
paul.thomas@dlr.de

Citation:

Thomas, P., Grott, M., Morschhauser, A., & Vervelidou, F. (2018). Paleopole reconstruction of Martian magnetic field anomalies. *Journal of Geophysical Research: Planets*, 123, 1140–1155. <https://doi.org/10.1002/2017JE005511>

Received 15 DEC 2017

Accepted 10 MAR 2018

Accepted article online 25 MAR 2018

Published online 11 MAY 2018

Paleopole Reconstruction of Martian Magnetic Field Anomalies

Paul Thomas¹ , Matthias Grott¹ , Achim Morschhauser², and Foteini Vervelidou² 
¹Department of Planetary Physics, German Aerospace Center, Berlin, Germany, ²Section 2.3 Geomagnetism, German Research Centre for Geosciences, Potsdam, Germany

Abstract The crust of Mars shows strong remanent magnetization, which was likely acquired during the early phases of planetary evolution when a core dynamo still operated. The direction of the field responsible for magnetizing the crust holds clues to the working of the dynamo and the rotational dynamics of the planet. By analyzing individual crustal magnetic field anomalies and with the aid of additional assumptions, the field orientations can be reconstructed. We have implemented an Equivalent Source Dipole method to determine the main field orientation during magnetization, assuming that the considered anomalies are unidirectionally magnetized without making specific assumptions about the source geometry. The available data are fit in a least squares sense, and the method yields confidence intervals for the admissible paleopole locations. The method was applied to six crustal magnetic field anomalies, two of which require a south pole in the northern hemisphere, while three indicate a south pole in the southern hemisphere. This implies that polar reversals took place at least once in Martian history. Furthermore, one of the investigated anomalies requires a south pole at equatorial to midlatitudes, indicating that a significant amount of true polar wander must have occurred on Mars. Finally, tests with synthetic data indicate that admissible paleopole locations typically spread across at least 25% of the planet, which may partially explain the scatter found in previously published paleopole studies.

Plain Language Summary Today, the crust of Mars is strongly magnetized, and magnetization was likely acquired when a core dynamo still operated. In this study, the crustal magnetization is investigated and inferences about the former global magnetic field are made. To this end, we have implemented a method to synthesize the local sources of crustal magnetization and determined the former main field orientation. The method was applied to six crustal magnetic field anomalies, two of which require a former magnetic south pole in the northern hemisphere, while three indicate a former magnetic south pole in the southern hemisphere. This implies that at least once in the Martian history the magnetic north and south poles switched places. Furthermore, one of the investigated anomalies requires a former magnetic south pole at equatorial to midlatitudes, indicating that the rotational axis of Mars must have altered its alignment significantly.

1. Introduction

The Mars flyby of Mariner 4 in 1965 indicated that present-day Mars does not possess an Earth-like main magnetic field (Smith et al., 1965), but even though magnetometer carrying spacecrafts approached Mars in the following decades, it was not until 1997 that the strong remanent magnetic field originating from the Martian crust was identified by the Mars Global Surveyor (MGS) mission (Acuña et al., 1999). MGS operated from 1997 to 2006 and provided the most complete survey of the Martian magnetic field to date, and while some data were gathered at altitudes below 200 km during the aerobraking and science phase orbits, the majority of the data were collected at a nearly constant altitude of 400 km during the mapping phase. New data are currently provided by the Mars Atmosphere and Volatile Evolution mission (Connerney, Espley, DiBraccio, et al., 2015; Connerney, Espley, Lawton, et al., 2015), but these remain to be integrated into magnetic field models.

Models of the magnetic field of Mars usually represent the field in terms of Equivalent Source Dipoles (ESD) (e.g., Langlais et al., 2004; Purucker et al., 2000) or spherical harmonic (SH) functions (e.g., Arkani-Hamed, 2001a, 2002; Morschhauser et al., 2014). The most recent global SH model is expanded up to degree and order 110 (Morschhauser et al., 2014), and local models have been expanded to degree and order 130

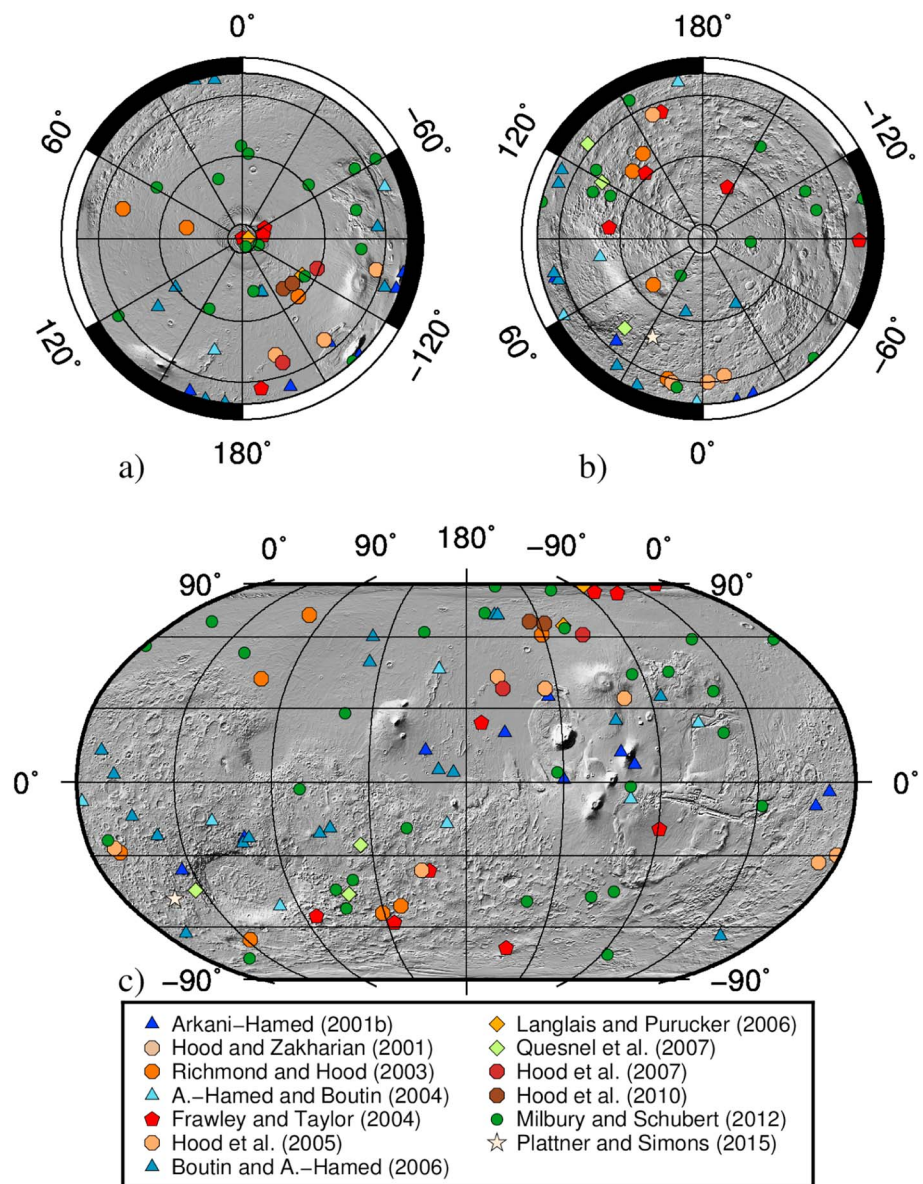


Figure 1. Compilation of published paleopole locations plotted on a shaded relief Mars Orbiter Laser Altimeter topographic map. All paleopole locations were converted into magnetic south pole positions. Stereographic projections of the northern and southern hemispheres are shown in the top row, while a global map in Robinson projection is shown at the bottom. Evidence for true polar wander has been reported by Boutin and Arkani-Hamed (2006), Frawley and Taylor (2004), Arkani-Hamed (2001b), Arkani-Hamed and Boutin (2004), Hood et al. (2007), Hood and Zakharian (2001), Hood et al. (2005), Langlais and Purucker (2006), Milbury et al. (2012), and Quesnel et al. (2007), while Boutin and Arkani-Hamed (2006), Frawley and Taylor (2004), Arkani-Hamed (2001b), Arkani-Hamed and Boutin (2004), and Milbury et al. (2012) in addition argue for at least one polar reversal event.

(Plattner & Simons, 2015). Using MGS data (Frawley & Taylor, 2004; Hood & Zakharian, 2001; Hood et al., 2005, 2007; Langlais & Purucker, 2006; Milbury et al., 2012; Quesnel et al., 2007; Richmond & Hood, 2003) or field models derived from these data (Arkani-Hamed, 2001b; Arkani-Hamed & Boutin, 2004; Plattner & Simons, 2015), a number of studies have tried to constrain the characteristics of the Martian core dynamo field during the Noachian period. Assuming that the main field was of dipolar character (Lillis et al., 2013), paleopole locations have been derived for a number of crustal magnetic field anomalies.

The results of these studies are summarized in Figure 1, where reported paleopole locations are plotted on a shaded relief topographic map and all locations have been converted to display magnetic south poles. While individual investigations reported some clustering of paleopole locations close to the Tharsis region

and at low latitudes (Arkani-Hamed, 2001b; Hood & Zakharian, 2001; Richmond & Hood, 2003), the compilation of results shows considerable spread. This has led many authors to argue that Mars underwent true polar wander (TPW) following the shutdown of the core dynamo (Boutin & Arkani-Hamed, 2006; Frawley & Taylor, 2004; Arkani-Hamed, 2001b; Arkani-Hamed & Boutin, 2004; Hood & Zakharian, 2001; Hood et al., 2005, 2007; Langlais & Purucker, 2006; Milbury et al., 2012; Quesnel et al., 2007), and some studies provide further evidence for polar reversal events (Arkani-Hamed, 2001b; Arkani-Hamed & Boutin, 2004; Boutin & Arkani-Hamed, 2006; Frawley & Taylor, 2004; Milbury et al., 2012).

However, such considerations only partially explain the large discrepancies between the reported locations, and it was soon suspected that different methods and assumptions made during modeling could significantly influence the obtained results (e.g., Boutin & Arkani-Hamed, 2006; Hood et al., 2007; Milbury et al., 2012; Tsunakawa et al., 2015). For simplicity, most methods for modeling crustal magnetic field anomalies assume that the magnetized region has elementary geometric shape, as this enables a derivation of closed expressions for the predicted field. Magnetic anomalies are therefore commonly modeled as circular or vertical prisms and spheres (Arkani-Hamed, 2001b; Hood & Zakharian, 2001; Hood et al., 2007; Quesnel et al., 2007), and the source geometry parameters are then varied to obtain the best fit to the magnetic field observations. However, the observed field could in principle be the result of an infinite number of differently shaped sources (Blakely, 1996; Telford et al., 1990), and since underlying assumptions regarding source location and shape influence the obtained results, methods that make less restrictive *a priori* assumptions should be preferred. The fact that usually only best fitting paleopole locations are reported without stating confidence limits for the obtained results further complicates the comparison between different studies. The accuracy of paleopole estimates was recently investigated by Vervelidou, Lesur, Morschhauser, et al. (2017), and it was shown that common methods for paleopole inversions introduce strong implicit assumptions concerning the null space as well as the full spectral content of the magnetization distribution. It was concluded that paleopole location estimates are only correct as long as the underlying assumptions, whether implicit or explicit, are not violated (Vervelidou, Lesur, Morschhauser, et al., 2017). Investigations following this approach are those of Parker (1991) and Oliveira and Wiczorek (2017).

In this study we chose an ESD method that is based on the assumption of unidirectional magnetization. Our implementation of the ESD method follows the derivation of Parker (1991), which is based on the general ESD approach of Mayhew (1979) for synthesizing magnetic sources with avoidance of making assumptions about the source geometry. Furthermore, it provides a measure of misfit for a given solution, such that confidence limits for the calculated paleopole locations can be derived. Parker's method assumes that the observed magnetic anomaly is generated by a unidirectional magnetization distribution, as would, for example, be acquired by material cooling through its Curie temperature in the presence of an inducing magnetic field, assuming that the direction of the latter remains constant during formation. Over small distances, this process generates magnetization that is almost unidirectional (see, e.g., Figure 1 of Vervelidou, Lesur, Morschhauser, et al., 2017).

In the following, we first introduce Parker's method in section 2, and our approach to derive the range of admissible paleopole locations are discussed. The method is then applied to synthetic test cases in section 3, where the prerequisites for successfully applying the method are analyzed. Finally, we apply the method to Martian magnetic field anomalies in section 4 and discuss the implications for the dynamics of the Martian core dynamo in section 5. Details of derivations and coordinate transformations are given in Appendices A and B.

2. Method

In this section we present a method to constrain the orientation of a centrally generated core dynamo field of dipolar character by analyzing isolated crustal magnetic field anomalies. In order to compare the modeled field with observations, we use the spherical harmonics representation of the crustal magnetic field derived by Morschhauser et al. (2014), which is based on MGS satellite data. The model is expanded to SH degree and order 110 and has been regularized by minimizing the L1 norm of the horizontal gradient of the vertically down component of the field at surface altitude. The model is characterized by low noise and is robust when downward continued to the surface. The magnetic field at a given location is given by

$$\mathbf{B}_{\text{sh}}(\theta, \phi, h) = -\nabla \left(a \sum_{l=1}^L \left(\frac{a}{h} \right)^{(l+1)} \sum_{m=-l}^l g_l^m Y_l^m(\theta, \phi) \right) \quad (1)$$

where $Y_l^m(\theta, \phi)$ denotes the Schmidt seminormalized SH functions, which depend on latitude θ and longitude ϕ . h is the observation radius, $a = 3,393.5$ km is the reference radius of the model, l and m are degree and order of the respective SH functions, $L = 110$ is the degree of the expansion, and g_l^m is the Gauss coefficient as provided by Morschhauser et al. (2014). Using equation (1), the field can be evaluated at any location \mathbf{r}_j .

To model a given crustal anomaly, a number of N dipoles is distributed at locations \mathbf{s}_i in the study area and all dipoles share a common magnetic orientation $\hat{\mathbf{m}}$ (Parker, 1991). Each dipole has a magnetic moment $\mathbf{m}_i = M_i \hat{\mathbf{m}}$, and the magnetic field generated at a location \mathbf{r}_j is then given by (e.g., Blakely, 1996)

$$\mathbf{B}(\mathbf{r}_j) = \frac{\mu_0}{4\pi} \sum_{i=1}^N \frac{M_i}{|\mathbf{r}_j - \mathbf{s}_i|^5} (3(\mathbf{r}_j - \mathbf{s}_i)[\hat{\mathbf{m}} \cdot (\mathbf{r}_j - \mathbf{s}_i)] - \hat{\mathbf{m}}|\mathbf{r}_j - \mathbf{s}_i|^2) \quad (2)$$

where μ_0 is the magnetic permeability in vacuum and the sum extends over all dipole contributions to the observed field. By evaluating the field at K locations \mathbf{r}_j , a linear system of equations is obtained, which may be rearranged in matrix form (compare Appendix A; also, see Aster et al., 2013) to solve for the N unknown magnetization strengths $\mathbf{M} = [M_1, M_2, \dots, M_N]^T$ and

$$\mathbf{M} = (\mathbf{G}^T \mathbf{G})^{-1} \mathbf{G}^T \mathbf{B} \quad (3)$$

As the magnetization is assumed to be uniform with $M_i \geq 0$ (Parker, 1991), we choose to solve equation (3) using the nonnegative least squares algorithm by Lawson and Hanson (1974). As shown by Parker (1991), an optimized solution can be achieved with only a subset of the N dipoles being different from 0. In general, increasing N will not increase accuracy of the results and we choose $N = K$ in the following.

In order to determine the best fitting magnetization direction $\hat{\mathbf{m}}$, the determination of \mathbf{M} is repeated for all possible magnetic orientations on the unit sphere, with inclination I between 0° and 180° and declination D between 0° and 360° . Increments of 1° in I and 2° in D have been used. This results in a total of 32,761 possible orientations, and the respective model misfits are calculated using

$$\sigma(\hat{\mathbf{m}}) = \sqrt{\frac{1}{K} \left(\sum_{i=1}^K \mathbf{B}_{sh} - \mathbf{G}(\hat{\mathbf{m}}) \cdot \mathbf{M} \right)^2} \quad (4)$$

Note that the above calculations can be performed using a single component of the vector magnetic field, and Parker (1991) projected $\mathbf{B}(\mathbf{r}_j)$ onto the main field direction. Here we choose a projection onto one of the main axes of the local coordinate system (north, east, and down) such that the signal-to-noise ratio (SNR) is maximized. For the anomalies investigated here, this direction is the downward pointing component B_z of the field in four out of six cases, consistent with the fact that this component usually is strongest and less noisy when compared to the north and east components (Morschhauser et al., 2014).

To determine the range of admissible models and thus admissible magnetization directions $\hat{\mathbf{m}}$, a threshold misfit I_{\min} needs to be defined, and admissible directions are then characterized by $\sigma(\hat{\mathbf{m}}) \leq I_{\min}$. Ideally, I_{\min} would be defined based on an analysis of the SH model's covariance matrix (Morschhauser et al., 2014), but in practice the correlations between the Gauss coefficients result in error estimates which are either too large or unrealistically small to be useful, depending on whether the whole covariance matrix or only its diagonal terms are used. Therefore, a different approach based on the method and lunar application by Oliveira and Wiczeorek (2017) was implemented here.

The chosen approach is based on the fact that Parker's method assumes uniform magnetic orientation in the study area, and any deviations from uniformity will be treated as noise in the following. Two main sources of noise are considered here: One represents a random component of small wavelength background magnetization that is present in the study area. The second component represents coherent fields which are caused by anomalies in the vicinity. The noise level for a given anomaly, that is, the maximum allowable misfit I_{\min} between admissible models and data, is then calculated as illustrated in Figure 2. After first picking the visual center location of the anomaly, a regular 3° by 3° grid with 1° spacing is generated. For each of the 49 grid points, $I(R)$ is then determined by averaging the relevant component of \mathbf{B}_{sh} in an annulus around the respective center. Averaging is done in steps of 0.5° , corresponding to ~ 30 km at the equator. The center location of the anomaly is then fixed by selecting the grid point for which I_{\min}^n , $1 \leq n \leq 49$, is minimal. I_{\min} then defines

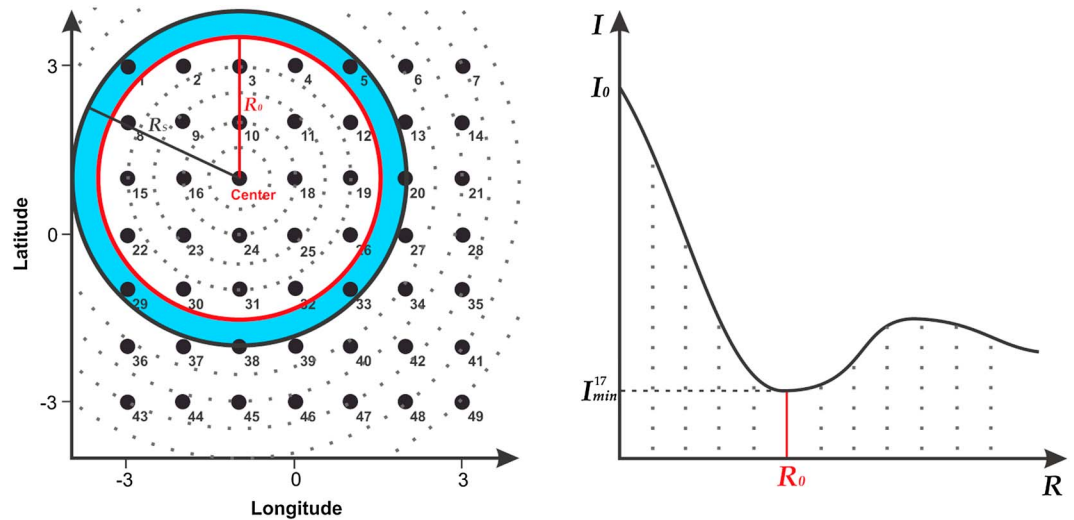


Figure 2. Illustration of the method to determine the confidence limit I_{\min} . In this example the visual center of the anomaly is located at point 25, and a regular 3° by 3° grid with 1° spacing is generated around the anomaly. For each grid point, $I(R)$ is determined as shown on the right-hand side of the figure by calculating the root-mean-square of the magnetic field within rings (blue) of increasing radii (dotted circles). The center of the anomaly is then chosen to be the grid point for which I_{\min}^n , $1 \leq n \leq 49$, is minimal. I_{\min} , R_0 (red circle), and R_s (black circle) are then determined for this center location.

the radius R_0 of the anomaly, which in turn corresponds to the radius of the respective dipole distribution. Accordingly, the SNR is given by

$$\text{SNR} = I_0 / I_{\min} \quad (5)$$

where I_0 is the average of B_{sh} for $R < 0.5^\circ$.

The N dipole locations \mathbf{s}_i are given by a homogeneous distribution of locations on a hexagonal grid within R_0 , and all dipoles are placed at surface altitude. Further, the magnetic field is evaluated at K locations \mathbf{r}_j , which are homogeneously distributed on a hexagonal grid within $R_s = R_0 + 1^\circ$. We choose an observation altitude of 120 km, close to the aerobraking phase orbit height.

The hexagonal distribution of dipoles is generated in the local north-east-down coordinate system by first placing one dipole in the center of the anomaly and then distributing six dipoles with an angular separation of 60° on a circle with radius R_0 . For each new dipole, six additional dipoles are then distributed in the same way but using the radius $R_0/2$. This process is repeated for decreasing radii until the desired resolution is reached. In this way, an equal area distribution of dipoles is generated, and we choose a distribution consisting of 241 dipoles. This corresponds to a spatial resolution of about 75 km near the equator for $R_0 = 10^\circ$.

As a final step, the magnetic orientations $\hat{\mathbf{m}}$ are converted to magnetic south pole positions taking the center location of the anomaly into account (see, e.g., Butler, 1992; also, see Appendix B). In this way, the uncertainty associated with the magnetic orientations $\hat{\mathbf{m}}$ can be associated with an uncertainty for the paleopole locations. To quantify the range of admissible paleopole locations, we estimate the area for which paleopole solutions have misfits smaller than I_{\min} and express this as a percentage in terms of the total Martian surface area. This then indicates the areal extent to which the paleopole locations can be constrained.

It should be pointed out that the above method assumes a uniform magnetic orientation and not necessarily a constant paleopole location for the dipoles considered. Therefore, the calculated paleopole location slightly varies with distance from the center of the observed anomaly. This implies that the above method works best for small anomalies like those observed on the Moon (Oliveira & Wiczorek, 2017) but will yield a conservative upper estimate for admissible paleopole locations when crustal magnetic field anomalies of larger spatial extent are considered.

3. Synthetic Tests and Sensitivity Analysis

To verify the above method, it was first tested if the implemented algorithm is capable of retrieving the magnetic orientation of a magnetic source consisting of a single dipole. For this test, the magnetic field generated

Table 1
Results of Synthetic Tests Considering an Anomaly at 0°N and 180°E for a Paleopole at the Same Location

#	Case	Distance	Noise	σ_{\min} (nT)	B_{\max} (nT)	I_{\min} (nT)	SNR	Area
1	-	-	0%	0.05	290.7	1.9	121/1	0%
1	-	-	5%	3.6	304.6	3.9	78/1	3.4%
1	-	-	10%	16.8	319.8	17.0	19/1	5.8%
1	-	-	25%	45.9	335.6	47.8	7/1	23.7%
2	AL	5°	0%	15.6	282.8	49.2	6/1	42.7%
2	TPW	5°	0%	14.6	283.9	45.7	6/1	42.0%
2	PR	5°	0%	14.3	298.6	49.8	6/1	41.7%
2	AL	7.5°	0%	2.35	287.5	11.5	25/1	27.2%
2	TPW	7.5°	0%	2.43	287.9	11.5	25/1	27.1%
2	PR	7.5°	0%	1.4	294.0	9.7	30/1	26.3%

Note. The number of considered anomalies (#), the orientation of the perturbing anomaly (Cases: AL = aligned; PR = opposite; TPW = 30° smaller inclination), the distance between primary and perturbing anomaly (Distance), and the amount of background noise (Noise) are given along with the corresponding minimum misfit (σ_{\min}), the maximum field strength (B_{\max}), the confidence limit threshold (I_{\min}), the signal-to-noise ratio (SNR), and the surface area coverage of admissible locations (Area).

by a single dipole of known magnetic orientation $\hat{\mathbf{m}}$ placed onto the surface was calculated at N observation points \mathbf{r}_j . $K = N$ dipoles were placed at locations \mathbf{s}_j , and the best fitting model was determined. In the absence of noise, the method then perfectly recovered the input orientation $\hat{\mathbf{m}}$. As a second test, the investigated anomaly was generated by a distribution of dipoles with uniform orientation, assuming a Gaussian distribution of magnetization strengths. Again, dipoles and observation points were distributed according to section 2 and the input orientation could be exactly retrieved.

To assess how a background field of random orientation affects the inferred paleopole location, a test case consisting of 241 equally distributed dipoles was constructed. The radius of the anomaly was chosen to be 2.5°, such that dipoles have a distance of 18.5 km. The center of the simulated magnetic anomaly was located at 0°N and 180°E, and all dipoles shared a common magnetic orientation of inclination 90° and declination 0°, corresponding to a paleopole location at the center of the anomaly (compare Appendix B). The magnetization strengths of the dipoles were chosen such that the field intensity at the center of the anomaly was close to 300 nT. Magnetization strengths were assumed to decline as a function of center distance according to a Gaussian distribution, and the standard deviation was chosen such that the field strength was 10% of the center strength at a distance of 2.5°. The magnetic field at 241 observation points was then calculated as outlined in section 2, and random noise was added to all components of the magnetic field. Four cases corresponding to 0%, 5%, 10%, and 25% random noise with respect to the maximum field strength were calculated.

In a final test, the anomaly described earlier was perturbed by placing an identical anomaly at distances of 5° and 7.5°. For each distance, three magnetic orientations were considered: First, the perturbing anomaly was chosen to have the same magnetic orientation (AL); second, the anomaly had opposite magnetic orientation (PR); and third, the inclination was changed by 30° with respect to the first anomaly (TPW). These cases were chosen to represent anomalies created during phases of similar main field geometry (aligned, first case), after a polar reversal event (second case), or after a TPW event (third case), which should reasonably bound the range of situations expected to be encountered on Mars. Results of the calculations are summarized in Table 1 where the different test cases are characterized by the number of considered anomalies (#), the orientation of the perturbing anomaly (Case), the distance between primary and perturbing anomaly (Distance), and the amount of background noise (Noise). As a result, the corresponding minimum misfit (σ_{\min}), the maximum field strength (B_{\max}), the confidence limit threshold (I_{\min}), SNR, and the surface area coverage of admissible locations are given (Area).

As is evident from Table 1, increased random noise increases the minimum attainable misfit σ_{\min} as well as the confidence limit threshold I_{\min} for isolated anomalies. As a consequence, the areas of admissible paleopole locations increase significantly once noise levels reach 10%. For 25% noise, areas of admissible paleopole

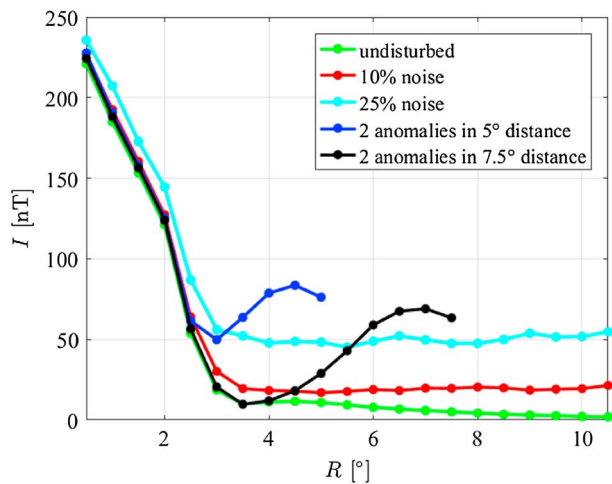


Figure 3. The confidence limit threshold as a function of radius for five representative test cases. Results for single anomalies with no (green), 10% (red), and 25% (cyan) added noise are shown along with cases considering two anomalies oriented opposite to one another (PR case of Table 1) and separated by 5° (blue) and 7.5° (black) of longitude.

locations extend over almost 25% of the planet, and in this case a fit to the data becomes almost impossible as σ_{\min} grows to be of the same order as the confidence limit threshold I_{\min} .

If a second perturbing anomaly is located at a distance of 5° from the main anomaly, the ability to constrain paleopole locations strongly deteriorates. First of all, the confidence limit threshold I_{\min} increases to values close to 50 nT, and second, the minimum attainable misfit grows to ~ 15 nT. As a consequence, paleopole locations can spread over $\sim 40\%$ of the planet. If, however, anomalies are separated by 7.5°, corresponding to three times their radius, the areal coverage of admissible locations decreases and paleopoles can be constrained to be within 25% of the planet's surface. In the above calculations, the B_z (down) component of the magnetic field has been used in the inversions, but tests using the B_x (north), or east B_y (east) component of the field show similar trends at decreased SNR (not shown).

Taken together, these results indicate that anomalies should be separated from other anomalies by least 2 times their radius to apply the above method. Furthermore, the magnetization direction of a second perturbing anomaly seems to be of secondary importance (compare the AL, TPW, and PR cases in Table 1). While added noise primarily acts to increase the misfit between the model and the observations, perturbing anomalies primarily

increase the confidence limit threshold I_{\min} . This is due to the fact that the inversion algorithm partially fits the disturbing (coherent) field but not the random noise.

To further illustrate the above results, the radially averaged mean magnetic field intensities of five test cases are shown in Figure 3, where the lines correspond to single anomalies with no (green), 10% (red), and 25% (cyan) added noise, as well as two cases considering anomalies oriented opposite one another (PR case of Table 1) and separated by 5° (blue) and 7.5° (black) in longitude. As is evident from the figure, added noise

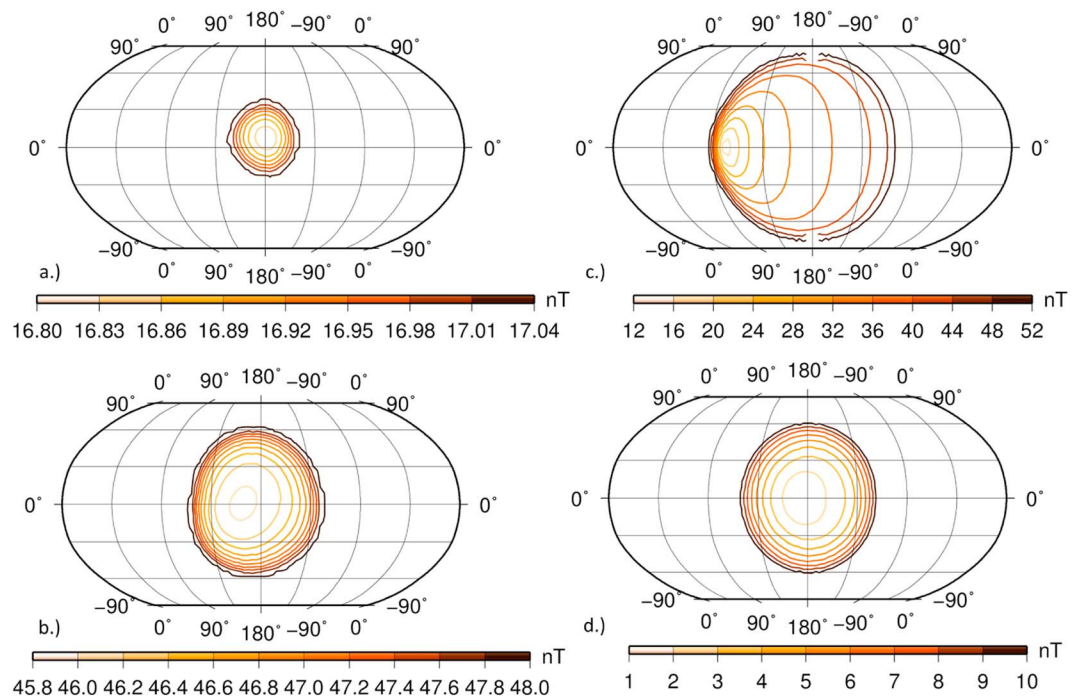


Figure 4. Contour plots of the model misfit for four representative test cases. The center of the anomaly equals the true pole location at 0°N and 180°E. Contour lines are plotted up to the confidence limit threshold I_{\min} for the respective test case. (a) Single anomaly with 10% random noise added to the data. (b) Single anomaly with 25% random noise added to the data. (c) Two anomalies separated 5° apart with opposing polarity. (d) Two anomalies separated 7.5° apart with opposing polarity.

significantly increases the level of background fields, while a second anomaly is visible as a second maximum in $I(R)$. In these examples, the radius R_0 should be chosen as far as feasible for the cases with added noise, while the best SNR for the 5° and 7.5° cases is obtained for R_0 equal to $\sim 3^\circ$ and $\sim 4^\circ$, respectively.

A graphical representation of admissible paleopole locations is shown in Figure 4, where contour plots of the misfit between model and observations are shown for test cases with 10% (a) and 25% (b) added random noise as well as for two anomalies separated 5° (c) and 7.5° (d) apart. While 10% added random noise results in a well-constrained paleopole location, the area coverage increases to 25% for the 25% noise case. This is similar to the result obtained for two anomalies separated 7.5° apart, corresponding to about 3 times their radius. However, it should be pointed out that for the 25% noise case the limiting factor constraining admissible locations is the ability to fit the data and thus the large fitting residual, while in the latter case the fit to the data is much better, but the background field is strong. Another interesting observation concerns the case with two anomalies separated 5° apart, where the presence of the second anomaly systematically introduces a bias toward its own location.

4. Results

In the following, we apply the method outlined in section 2 to six crustal magnetic field anomalies which are particularly suited for such an investigation due to their high degree of isolation with respect to neighboring fields. Three of these anomalies were already identified and discussed by Morschhauser et al. (2014), and they are located close to the Green, South, and Tyndall craters, respectively. These will be denoted A1, A2, and A3 in the following. Another anomaly is associated with the Australe Montes volcano, which has been extensively discussed by Plattner and Simons (2015), and will be denoted A. Montes in the following. A global search for additional isolated magnetic field anomalies identified another 18 promising candidates, but only two of these turned out to have SNRs of more than 4/1. These are denoted P1 and P2 in the following, and they are located close to the Bouguer crater and in eastern Amazonis Planitia. The other candidate anomalies are disregarded.

Figure 5 shows maps of the B_x (north) and B_z (down) components of the magnetic field for the six considered crustal magnetic field anomalies. The magnetic field was calculated at an altitude of 120 km from the SH model of Morschhauser et al. (2014). Additionally, MGS aerobraking tracks between altitudes of 90 km and 130 km are shown where available. Further, the dipole distribution radii R_0 are indicated by red circles. Anomalies A2 and P2 have amplitudes of ~ 100 nT, A1 has an amplitude of ~ 60 nT, P1 has an amplitude of ~ 300 nT, and A3 and A. Montes have amplitudes of ~ 30 nT. As shown in the figure, anomalies are well isolated and stray fields have low amplitude at the radius R_0 .

Results of the paleopole inversion are summarized in Table 2, where the anomaly's name (Anomaly), the determined center location (Center location), the magnetic field component used for the inversion ($B_{x,y,z}$), and the dipole distribution radius (R_0) are given. In addition, the minimum misfit (σ_{\min}), maximum field strength (B_{\max}), confidence threshold (I_{\min}), SNR, and surface area coverage of admissible paleopole locations (Area) are shown. In the inversion, the B_z component has been used for anomalies A2, A. Montes, P1, and P2, while for anomalies A1 and A3 the highest SNR was obtained for the B_x component.

Determined center locations of anomalies A1, A2, A3, and P2 are in the midlatitudes, while A. Montes and P1 are located close to the pole and equator, respectively. The size of the anomalies varies between 4.5° and 18°, but since the total lateral extent depends on latitude, the radii of A. Montes and P2 both correspond to ~ 160 km (compare Table 2). The fits to the SH model are generally good, and residuals are below 5% with respect to the maximum field strength, resulting in misfits of only a few nanotesla. In this regard, anomaly P1 is an exception and residuals are of the order of 10% with respect to the main field strength, indicating the presence of unmodeled signal in the vicinity. Background noise is generally between 10% and 15% of the maximum field strength except for A. Montes, where noise is of the order of 25%, resulting in a low SNR.

Confidence limits for admissible paleopole locations vary strongly between the investigated anomalies, and the majority of cases show admissible areas which cover more than 40% of the planet, similar to some anomalies investigated on the Moon (Oliveira & Wieczorek, 2017). The tighter bounds estimated for A1 and P1 are a result of the relatively large misfits σ_{\min} , which are already of the order of the confidence limit threshold. Therefore, already small variations around the best fitting magnetization direction will result in unacceptable fits.

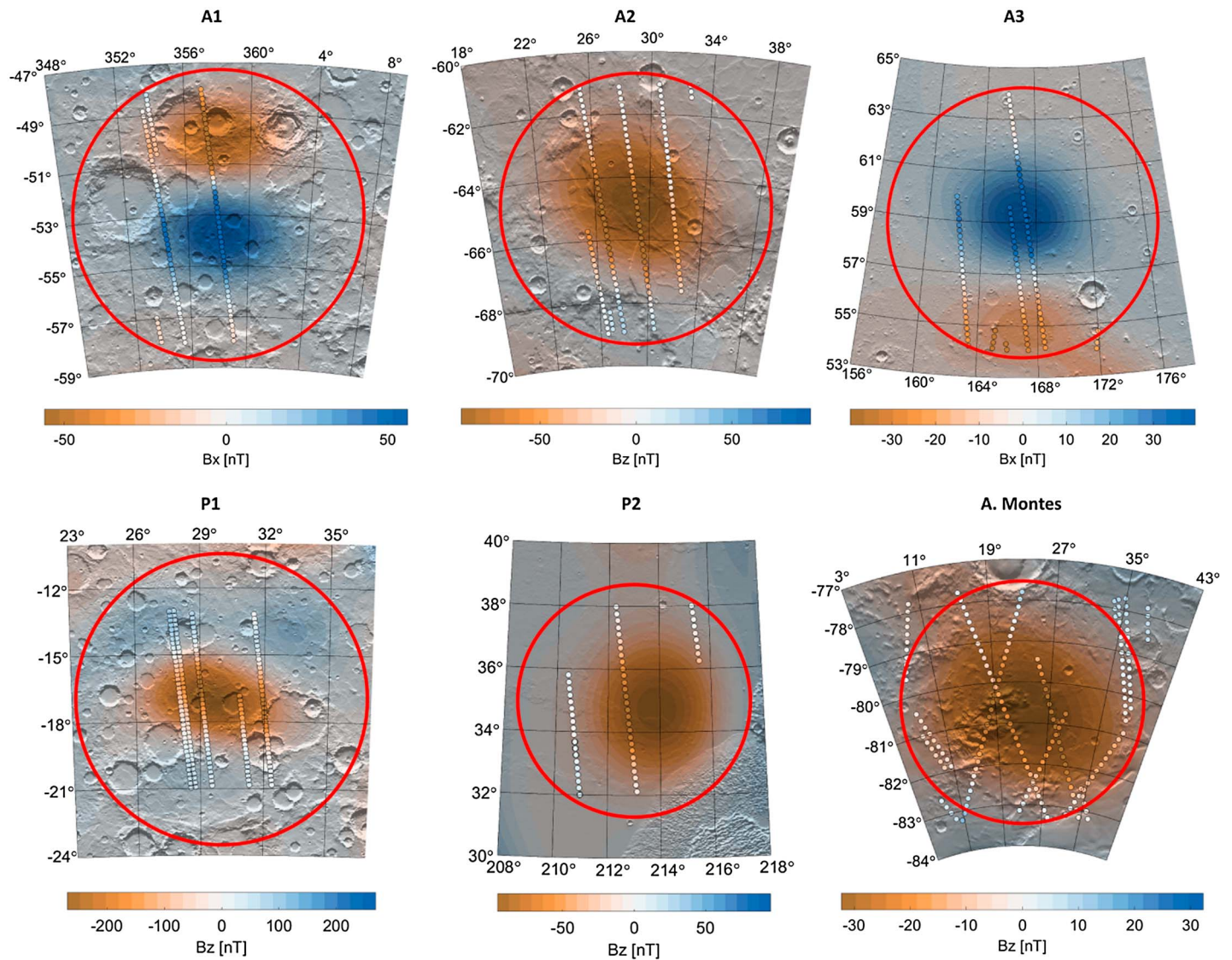


Figure 5. Color-coded field strength at an altitude of 120 km for six crustal magnetic field anomalies plotted over Mars Orbiter Laser Altimeter shaded relief topographic maps. Field strength was calculated from the Morschhauser et al. (2014) spherical harmonic model, and the field's B_z (down) component for A2, A. Montes, P1, and P2 as well as the field's B_x (north) component for A1 and A3 are shown. In addition, available Mars Global Surveyor aerobraking phase magnetic field data tracks are shown for altitudes between 90 km and 130 km. Note that all plots have individual color scale. The dipole distribution radius R_0 (red) is shown for reference.

Table 2

Results of the Inversion for Six Crustal Magnetic Field Anomalies

Anomaly	Center location	$B_{x,y,z}$	R_0	σ_{\min} (nT)	B_{\max} (nT)	I_{\min} (nT)	SNR	Area
A1	53°S/2°W	B_x	9.5°	3.1	56.0	3.6	12/1	9%
A2	64.5°S/28.5°E	B_z	10°	1.1	90.4	6.9	13/1	40%
A3	58.5°N/166.5°E	B_x	10°	1.8	39.1	5.8	7/1	46%
A. Montes	80.5°S/23.4°E	B_z	18°	0.4	32.2	8.4	4/1	57%
P1	16.5°S/30°E	B_z	6.5°	23.7	261.4	28.0	9/1	22%
P2	35°N/212.5°E	B_z	4.5°	3.6	94.5	11.7	7/1	40%

Note. Anomaly name (Anomaly), determined center location (Center location), magnetic field component used in the inversion ($B_{x,y,z}$), dipole distribution radius (R_0), minimum misfit (σ_{\min}), maximum field strength (B_{\max}), calculated confidence threshold (I_{\min}), signal-to-noise ratio (SNR), and the surface area coverage of admissible paleopole locations (Area) are given.

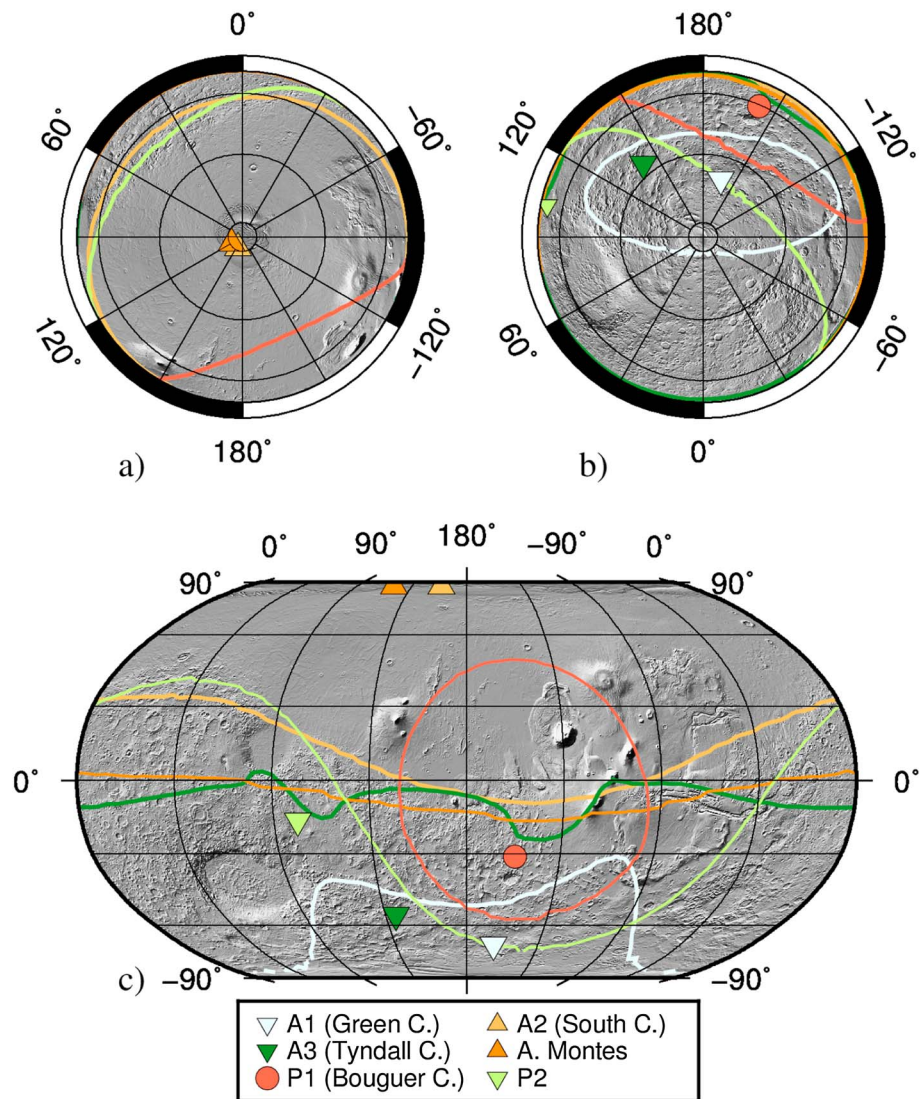


Figure 6. Admissible paleopole locations for six crustal magnetic field anomalies showing the best fitting paleopole location (compare Table C1) together with an estimate of the admissible location range. Contour lines enclose admissible paleopole locations and correspond to misfits equal to the threshold value I_{\min} . Symbols indicate whether paleopole locations are located in the northern hemisphere (upward pointing triangles), in the southern hemisphere (downward pointing triangle), or at midlatitudes excluding the poles (circles). Anomalies A2 and A. Montes therefore indicate paleopole locations in the northern hemisphere; A1, A3, and P2 indicate locations in the southern hemisphere, and P1 corresponds to midlatitude paleopole locations.

A graphical representation of the obtained inversion results is shown in Figure 6, where the ranges of admissible paleopole locations for the six crustal magnetic field anomalies are shown together with their best fitting paleopole location. Contour lines are reduced to the confidence limit threshold I_{\min} , and all solutions inside the contour are admissible. The inclination I , declination D , and best fitting paleopole locations are summarized in Table C1. For A1, admissible paleopole locations cover 9% of the Martian surface (white line), pointing toward a former magnetic south pole in the higher southern latitudes. In comparison, A2 (yellow line) covers an area of about 40% in the northern hemisphere, with the contour following the Martian crustal dichotomy boundary and indicating a former magnetic south pole in this area. For A3 (dark green line), the confidence limit extends over 46% of the surface, covering almost the entire southern hemisphere and indicating a magnetic south pole on this hemisphere of Mars. For P2 (light green line), paleopoles are constrained to 40% of the planet, excluding the Tharsis region but extending from the south pole to middle northern latitudes. The former magnetic south pole corresponding to this anomaly can thus not be constrained to one hemisphere.

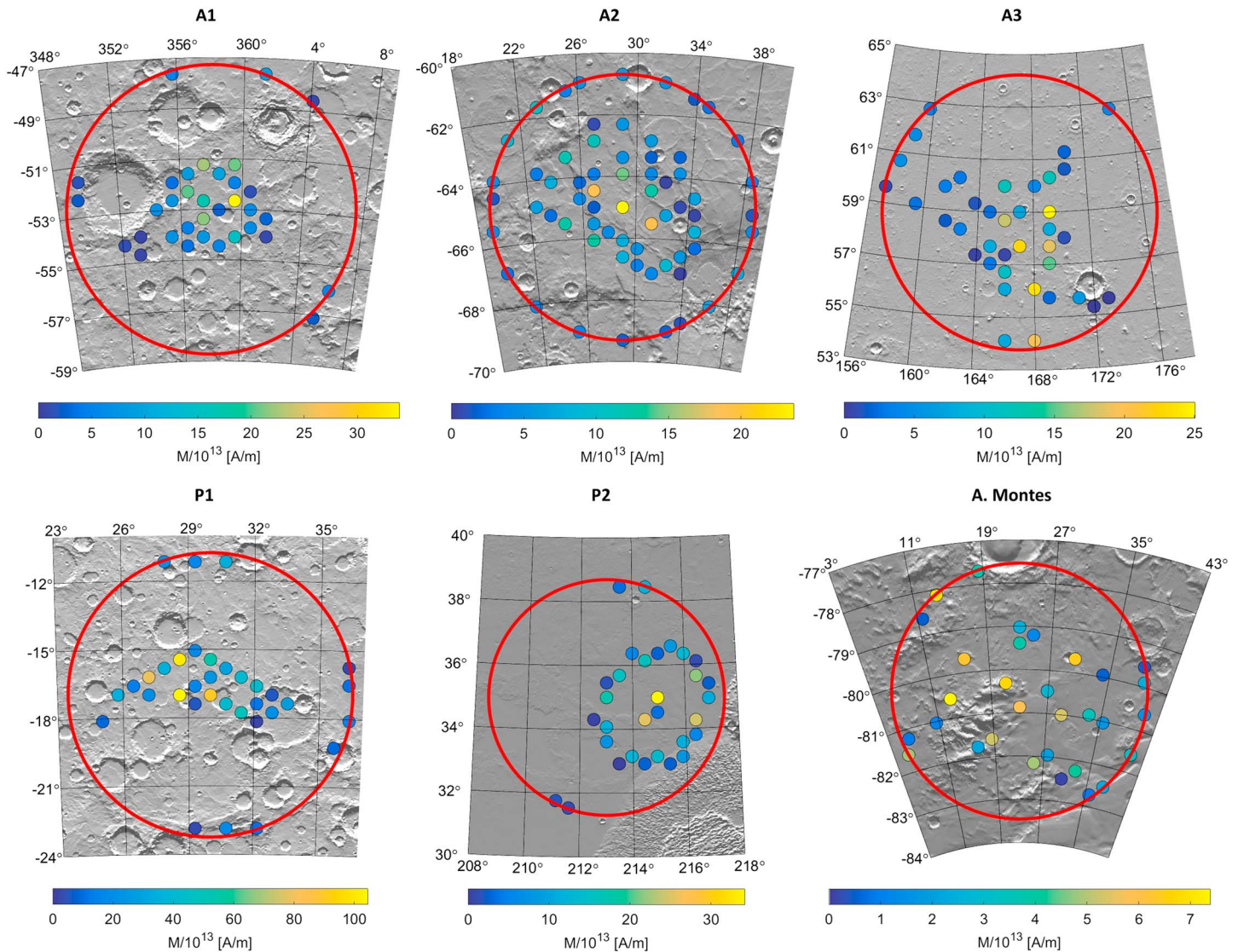


Figure 7. Results of the inversion showing color-coded representations of the dipoles' magnetization strengths $M_i > 0$ plotted over a Mars Orbiter Laser Altimeter shaded relief topographic map. Results for the best fitting models of anomalies A1, A2, A3, P1, P2, and A.Montes are shown. The red circles indicate the respective dipole distribution radii R_0 . Note that all maps have individual color scales.

For A. Montes (orange line), localization of paleopoles is constrained to the northern hemisphere, including a large fraction of the Tharsis province. This is compatible with the results obtained by Plattner and Simons (2015), who reported a clustering of potential pole locations around 48° northern latitude and 207° eastern longitude in between the Tharsis and Elysium provinces. Given the low SNR of the A. Montes anomaly from the global SH model, the comparison with the results of Plattner and Simons (2015) is satisfactory.

Anomaly P1 (red line) is an exception with respect to the range of admissible pole locations, as these do not include the geographic poles of Mars. Rather, the admissible area covers 22% of the planet, containing parts of the Tharsis region, Terra Sirenum, Terra Cimmeria, Amazonis Planitia, and Elysium Planitia. During the early evolution, the magnetic south pole of Mars must have been located in this region and was thus separated by at least 30° from the present-day geographic south pole. This indicates that a significant amount of TPW must have occurred on Mars.

Figure 7 shows a different representation of the inversion results, where the magnetization strengths M_i of individual model dipoles are shown for the best fitting solutions corresponding to the six studied anomalies. In Figure 7, magnetization strengths are plotted over Mars Orbiter Laser Altimeter shaded relief topographic maps, and the dipole distribution radii R_0 are shown in red for reference. As discussed in section 2,

the maximum number of dipoles with nonzero magnetization is usually smaller than the number of observation points N , and this is also observed in Figure 7. Magnetized dipoles cluster around the center of the investigated regions for anomalies A1, A2, and P1, with decreasing magnetization as a function of center distance. For A3, magnetized dipoles show a more complex structure, the magnetized region has a band shape crossing the investigation region, and paleopole estimates should be handled with more caution. However, magnetization generally decreases with increasing center distance and the derived area of admissible paleopole locations is not unrealistically small to be unreliable. For P2, the center of magnetization is shifted toward the eastward direction, indicating that investigation region and anomaly center are offset. However, due to the presence of perturbing anomalies toward the southeast, shifting the investigation region would result in lower SNR and not improve the results. For A. Montes, nonzero magnetization spreads over the entire investigation region, as might be expected for such a weak and spatially extended anomaly. It might therefore be the least suitable candidate for this investigation. It is also worth pointing out that a good localization of magnetized dipoles toward the center of the investigated region seems to correlate with a high SNR, as is observed for anomalies A1, A2, and P1. In this case, the assumption of uniform magnetization can fit the data well, and nonmodeled contributions to the observed magnetic field are small.

5. Summary and Conclusions

We have implemented Parker's (1991) method to investigate the admissible range of paleopole locations associated with Martian crustal magnetic field anomalies. The method assumes a uniform magnetic orientation in the investigated region and determines the magnetic orientation best compatible with observations. A grid of dipoles is distributed in the investigation region, and magnetization strengths of the dipoles are determined using a nonnegative least squares algorithm (Lawson & Hanson, 1974) to obtain the best fitting solution for a given magnetic orientation. By varying orientations, a measure of misfit is obtained and all orientations yielding a misfit lower than a given threshold are deemed admissible. As the uncertainty associated with the magnetic field measurements themselves is usually small, field contributions not covered by the assumption of uniform magnetization will govern the attainable minimum misfit, and we require the fits to be better than the average background field present in the region. It is worth noting that deriving paleopole locations assumes that the observed anomalies formed in the presence of a centrally generated dipole field, as is likely given the strength of magnetic anomalies observed on the Martian surface (Lillis et al., 2013). However, a single-hemisphere dynamo generating a weak field in the northern plains cannot be ruled out (Stanley et al., 2008).

Sensitivity tests of the implemented method show that the calculated best fitting paleopole locations strongly depend on the presence of background noise and perturbations due to adjacent anomalies. Best results are obtained for SNR above 10, that is, for anomalies whose strength is 10 times the background field or higher. Nevertheless, admissible paleopole locations usually spread over 25% of the planet's surface even for well-isolated anomalies. Out of the six crustal magnetic field anomalies investigated here, paleopole positions associated with four anomalies cannot be constrained to better than 40% of the planet.

Nevertheless, obtained results clearly show that magnetic south poles can be constrained to the northern as well as the southern hemisphere, respectively. Magnetic orientations of anomalies A1, A3, and P2 are compatible with magnetic south poles in the southern hemisphere, while anomalies A2 and A. Montes require magnetic south pole positions in the northern hemisphere. This indicates that at least one polar reversal event took place in Martian history, as has been previously reported (Arkani-Hamed, 2001b; Arkani-Hamed & Boutin, 2004; Boutin & Arkani-Hamed, 2006; Frawley & Taylor, 2004; Milbury et al., 2012). For the anomalies investigated here, the best localization was obtained for A1, indicating pole locations in the high southern latitudes. The frequency of polar reversal events cannot be retrieved from the present data, as most anomalies are not associated with geological surface features that could help to date them. In addition, dating the surface does not necessarily date the underlying magnetic anomaly, such that rock samples of known magnetic orientation and location would be necessary to gain insight into the detailed dynamics of the core dynamo.

Results obtained for anomaly P1 are not compatible with an axially oriented core dynamo and the position of the present-day rotational axis. Admissible paleopole locations for P1 only extend to 60°S, indicating that TPW (Bouley et al., 2016; Kite et al., 2009) of about 30° must have occurred on Mars. TPW has previously been suggested by Arkani-Hamed (2001b), Hood and Zakharian (2001), Arkani-Hamed and Boutin (2004), Frawley and Taylor (2004), Hood et al. (2005), Boutin and Arkani-Hamed (2006), Langlais and Purucker (2006),

Quesnel et al. (2007), Hood et al. (2007), and Milbury et al. (2012), and Bouley et al. (2016) constrained the amount of TPW associated with the Tharsis rise to 20° to 25°. This is only slightly smaller than the amount of TPW estimated here and may be consistent considering that rotational axis and dipole axis do not necessarily need to coincide. Results are thus compatible with a Tharsis-driven reorientation before the dynamo shutdown at around 4.1 Gyr (Lillis et al., 2013; Vervelidou, Lesur, Grott, et al., 2017).

Due to the large spread of admissible locations, the clustering of paleopoles close to the Tharsis region and at low latitudes as reported by Arkani-Hamed (2001b), Hood and Zakharian (2001), and Richmond and Hood (2003) could not be confirmed here. However, results obtained for A2, A3, and A. Montes are compatible with low-latitude solutions, while anomaly P1 allows for pole locations in the Tharsis region. Therefore, admissible pole locations reflect the spread of paleopole locations found by other authors, and it seems likely that paleopole location uncertainties have previously been underestimated.

The obtained areas of admissible paleopole locations calculated here are relatively large, but it seems unlikely that much tighter bounds can be derived from the presently available data. Even using a local model, Plattner and Simons (2015) could not constrain the range of admissible paleopole locations corresponding to the A. Montes magnetic anomaly to be better than ~70° in latitude, which is only slightly smaller than the uncertainty range estimated here. Therefore, better resolved low-altitude data will be necessary to put more stringent constraints on Martian paleopole locations, and these may become available through the currently operating Mars Atmosphere and Volatile EvolutionN mission (Connerney, Espley, Lawton, et al., 2015).

Appendix A: Determination of G

Given a dipole at location \mathbf{s}_i with magnetization $\mathbf{m}_i = M_i \hat{\mathbf{m}}_i$, the magnetic field \mathbf{B}_i at the location \mathbf{r}_j can be calculated using equation (2). In matrix form, this can be rewritten as

$$\mathbf{B}_i(\mathbf{r}_j) = \mathbf{A}_{ji}(\mathbf{r}_j, \mathbf{s}_i) \mathbf{m}_i \quad (\text{A1})$$

where

$$\mathbf{A}_{ji}(\mathbf{r}_j, \mathbf{s}_i) = \frac{\mu_0}{4\pi \cdot \Delta r_{ji}^5} \begin{pmatrix} 3(r_j^x - s_i^x)^2 - \Delta r_{ji}^2 & 3(r_j^x - s_i^x)(r_j^y - s_i^y) & 3(r_j^x - s_i^x)(r_j^z - s_i^z) \\ 3(r_j^x - s_i^x)(r_j^y - s_i^y) & 3(r_j^y - s_i^y)^2 - \Delta r_{ji}^2 & 3(r_j^y - s_i^y)(r_j^z - s_i^z) \\ 3(r_j^x - s_i^x)(r_j^z - s_i^z) & 3(r_j^y - s_i^y)(r_j^z - s_i^z) & 3(r_j^z - s_i^z)^2 - \Delta r_{ji}^2 \end{pmatrix} \quad (\text{A2})$$

Here $\Delta r_{ji} = |\mathbf{r}_j - \mathbf{s}_i|$ and superscripts x, y , and z denote the components of the respective vectors. Now given N magnetic sources and K observation points, the above formulation can be generalized by rearranging the vectors \mathbf{r}_j and \mathbf{m}_i according to $\mathbf{r} = (\mathbf{r}_1, \dots, \mathbf{r}_K)^T$ and $\mathbf{m} = (M_1 \hat{\mathbf{m}}_1, \dots, M_N \hat{\mathbf{m}}_N)^T$. Then,

$$\mathbf{B}(\mathbf{r}) = \mathbf{F}(\mathbf{r}_1, \dots, \mathbf{r}_K, \mathbf{s}_1, \dots, \mathbf{s}_N) \mathbf{m} \quad (\text{A3})$$

where

$$\mathbf{F}(\mathbf{r}_1, \dots, \mathbf{r}_K, \mathbf{s}_1, \dots, \mathbf{s}_N) = \begin{pmatrix} \mathbf{A}_{11}(\mathbf{r}_1, \mathbf{s}_1) & \mathbf{A}_{12}(\mathbf{r}_1, \mathbf{s}_2) & \dots & \mathbf{A}_{1N}(\mathbf{r}_1, \mathbf{s}_N) \\ \mathbf{A}_{21}(\mathbf{r}_2, \mathbf{s}_1) & \mathbf{A}_{22}(\mathbf{r}_2, \mathbf{s}_2) & \dots & \mathbf{A}_{2N}(\mathbf{r}_2, \mathbf{s}_N) \\ \dots & \dots & \dots & \dots \\ \mathbf{A}_{K1}(\mathbf{r}_K, \mathbf{s}_1) & \mathbf{A}_{K2}(\mathbf{r}_K, \mathbf{s}_2) & \dots & \mathbf{A}_{KN}(\mathbf{r}_K, \mathbf{s}_N) \end{pmatrix} \quad (\text{A4})$$

Assuming that all dipoles share a common magnetic orientation $\hat{\mathbf{m}}$, equation (A3) can be further simplified by defining $\mathbf{M} = (M_1, \dots, M_N)^T$. Then, we can define $\tilde{\mathbf{A}}_{ji}(\mathbf{r}_j, \mathbf{s}_i, \hat{\mathbf{m}}) = \mathbf{A}_{ji}(\mathbf{r}_j, \mathbf{s}_i) \hat{\mathbf{m}}$ and obtain

$$\mathbf{B}(\mathbf{r}) = \mathbf{G}(\mathbf{r}_1, \dots, \mathbf{r}_K, \mathbf{s}_1, \dots, \mathbf{s}_N, \hat{\mathbf{m}}) \mathbf{M} \quad (\text{A5})$$

with

$$\mathbf{G}(\mathbf{r}_1, \dots, \mathbf{r}_K, \mathbf{s}_1, \dots, \mathbf{s}_N, \hat{\mathbf{m}}) = \begin{pmatrix} \tilde{\mathbf{A}}_{11}(\mathbf{r}_1, \mathbf{s}_1, \hat{\mathbf{m}}) & \tilde{\mathbf{A}}_{12}(\mathbf{r}_1, \mathbf{s}_2, \hat{\mathbf{m}}) & \dots & \tilde{\mathbf{A}}_{1N}(\mathbf{r}_1, \mathbf{s}_N, \hat{\mathbf{m}}) \\ \tilde{\mathbf{A}}_{21}(\mathbf{r}_2, \mathbf{s}_1, \hat{\mathbf{m}}) & \tilde{\mathbf{A}}_{22}(\mathbf{r}_2, \mathbf{s}_2, \hat{\mathbf{m}}) & \dots & \tilde{\mathbf{A}}_{2N}(\mathbf{r}_2, \mathbf{s}_N, \hat{\mathbf{m}}) \\ \dots & \dots & \dots & \dots \\ \tilde{\mathbf{A}}_{K1}(\mathbf{r}_K, \mathbf{s}_1, \hat{\mathbf{m}}) & \tilde{\mathbf{A}}_{K2}(\mathbf{r}_K, \mathbf{s}_2, \hat{\mathbf{m}}) & \dots & \tilde{\mathbf{A}}_{KN}(\mathbf{r}_K, \mathbf{s}_N, \hat{\mathbf{m}}) \end{pmatrix} \quad (\text{A6})$$

Equation (A5) can then be inverted to yield

$$\mathbf{M} = (\mathbf{G}^T \mathbf{G})^{-1} \mathbf{G}^T \mathbf{B} \quad (\text{A7})$$

which is equation (3) given in section 2.

Appendix B: Paleopole Reconstruction

Given a dipole on the surface, the corresponding paleopole location can be calculated from the dipole's longitude Φ_s , latitude λ_s , and magnetic orientation $\hat{\mathbf{m}}$ (Butler, 1992). As a first step, dipole inclination I and declination D have to be calculated from the unit vector $\hat{\mathbf{m}}$, which for $-90^\circ \leq I \leq 90^\circ$ and $0^\circ \leq D \leq 360^\circ$ is defined as

$$\hat{\mathbf{m}} = \begin{pmatrix} e_x \\ e_y \\ e_z \end{pmatrix} \quad \text{with} \quad \begin{aligned} e_x &= \cos(I)\cos(D) \\ e_y &= \cos(I)\sin(D) \\ e_z &= \sin(I) \end{aligned} \quad (\text{B1})$$

Next, the magnetic colatitude p , that is, the great circle distance between the dipole's location and the paleopole position, needs to be determined. This is given by

$$p = \tan^{-1} \left(\frac{2}{\tan(I)} \right) \quad (\text{B2})$$

and care must be taken to account for negative values of p , for which 180° has to be added. Given the magnetic colatitude p , the paleopole latitude can be calculated according to

$$\Phi_p = \sin^{-1} [\sin(\Phi_s)\cos(p) + \cos(\Phi_s)\sin(p)\cos(D)] \quad (\text{B3})$$

As a next step, the longitudinal difference β between paleopole and dipole location is calculated. It is given by

$$\beta = \sin^{-1} \left(\frac{\sin(p)\sin(D)}{\cos(\Phi_p)} \right) \quad (\text{B4})$$

and two cases for the paleopole longitude λ_p need to be distinguished:

1. if $\cos(p) \geq \sin(\Phi_s)\sin(\Phi_p)$, then

$$\lambda_p = \lambda_s + \beta \quad (\text{B5})$$

2. if $\cos(p) < \sin(\Phi_s)\sin(\Phi_p)$, then

$$\lambda_p = \lambda_s + 180^\circ - \beta \quad (\text{B6})$$

Φ_p and λ_p then represent the looked for paleopole longitude and latitude.

Appendix C: Table of Best Fitting Results

Table C1 provides the determined best fitting magnetic orientations (I/D) in combination with the calculated paleopole locations, for the six observed crustal magnetic field anomalies. The listed pole latitudes and longitudes are further plotted in Figure 6 as triangles and circles to indicate hemispheric affiliation of the areas of admissible paleopole locations.

Table C1
Best Fitting Results for the Inversions of Six Crustal Magnetic Field Anomalies

Anomaly	I	D	Pole latitude	Pole longitude
A1	52°	188°	68°S	197°E
A2	−78°	8°	86°N	159°E

Table C1 (continued)

Anomaly	I	D	Pole latitude	Pole longitude
A3	−44°	196°	55°S	140°E
A. Montes	−85°	26°	87°N	120°E
P1	−61°	172°	31°S	203°E
P2	−45°	268°	16°S	101°E

Note. Anomaly name, determined inclination *I*, declination *D*, and the best fitting paleopole latitude and longitude are given.

Acknowledgments

This work has been supported by the Deutsche Forschungsgemeinschaft (DFG) through contracts GR 3751/1-2 and LE 2477/3-2 in the frame of the DFG priority program “Planetary Magnetism” (SPP 1488). All data necessary to reproduce the graphics shown in this paper are provided in the supporting information.

References

- Acuña, M. H., Connerney, J. E. P., Ness, N. F., Lin, R. P., Mitchell, D., Carlson, C. W., et al. (1999). Global distribution of crustal magnetization discovered by Mars Global Surveyor MAG/ER Experiment. *Science*, 284, 790–793.
- Arkani-Hamed, J. (2001a). A 50-degree spherical harmonic model of the magnetic field of Mars. *Journal of Geophysical Research*, 106(E10), 23,197–23,208. <https://doi.org/10.1029/2000JE001365>
- Arkani-Hamed, J. (2001b). Paleomagnetic pole positions and pole reversals of Mars. *Geophysical Research Letters*, 27(17), 3409–3412.
- Arkani-Hamed, J. (2002). An improved 50-degree spherical harmonic model of the magnetic field of Mars derived from both high-altitude and low-altitude data. *Journal of Geophysical Research*, 107(E10), 5083. <https://doi.org/10.1029/2001JE001835>
- Arkani-Hamed, J., & Boutin, D. (2004). Paleomagnetic poles of Mars: Revisited. *Journal of Geophysical Research*, 109, E03011. <https://doi.org/10.1029/2003JE002229>
- Aster, R. C., Borchers, B., & Thurber, C. H. (2013). *Parameter estimation and inverse problems* (2nd ed.). Waltham: Academic Press.
- Blakely, R. J. (1996). *Potential Theory in Gravity and Magnetic Applications*. Cambridge, UK: Cambridge University Press.
- Bouley, S., Baratoux, D., Matsuyama, I., Forget, F., Séjourné, A., Turbet, M., & Costard, F. (2016). Late Tharsis formation and implications for early Mars. *Nature*, 531, 344–347.
- Boutin, D., & Arkani-Hamed, J. (2006). Pole wandering of Mars: Evidence from paleomagnetic poles. *Icarus*, 181, 13–25.
- Butler, R. F. (1992). *Paleomagnetism: Magnetic Domains to Geologic Terranes*. Oxford: Blackwell Science.
- Connerney, J. E. P., Espley, J., Lawton, P., Murphy, S., Odom, J., Oliverson, R., & Sheppard, D. (2015). The MAVEN magnetic field investigation. *Space Science Reviews*, 195, 257–291. <https://doi.org/10.1007/s11214-015-0169-4>
- Connerney, J. E. P., Espley, J. R., DiBraccio, G. A., Gruesbeck, J. R., Oliverson, R. J., Mitchell, D. L., et al. (2015). First results of the MAVEN magnetic field investigation. *Geophysical Research Letters*, 42, 8819–8827. <https://doi.org/10.1002/2015GL065366>
- Frawley, J. J., & Taylor, P. T. (2004). Paleo-pole positions from Martian magnetic anomaly data. *Icarus*, 172, 316–327.
- Hood, L. L., Harris, K. P., Langlais, B., Lillis, R. J., Poulet, F., & Williams, D. A. (2010). Magnetic anomalies near Apollinaris Patera and the Medusae Fossae Formation in Lucus Planum, Mars. *Icarus*, 208, 118–131.
- Hood, L. L., Richmond, N. C., Harris, K. P., & Lillis, R. J. (2007). East west trending magnetic anomalies in the southern hemisphere of Mars: Modeling analysis and interpretation. *Icarus*, 191, 113–131.
- Hood, L. L., Young, C. N., Richmond, N. C., & Harris, K. P. (2005). Modeling of major Martian magnetic anomalies: Further evidence for polar reorientations during Noachian. *Icarus*, 177, 144–173.
- Hood, L. L., & Zakharian, A. (2001). Mapping and modeling of magnetic anomalies in the northern polar regions of Mars. *Journal of Geophysical Research*, 106, 601–619.
- Kite, E. S., Matsuyama, I., Manga, M., Perron, J. T., & Mitrovica, J. X. (2009). True polar wander driven by late-stage volcanism and the distribution of paleopolar deposits on Mars. *Earth and Planetary Science Letters*, 280(2009), 254–267.
- Langlais, B., & Purucker, M. E. (2006). A polar magnetic paleopole associated with Apollinaris Patera, Mars. *Planetary and Space Science*, 55, 270–279.
- Langlais, B., Purucker, M. E., & Manda, M. (2004). Crustal magnetic field of Mars. *Journal of Geophysical Research*, 109, E02008. <https://doi.org/10.1029/2003JE002048>
- Lawson, C. L., & Hanson, R. J. (1974). *Solving least squares problems*. Englewood Cliffs: Prentice-Hall.
- Lillis, R. J., Robbins, S., Manga, M., Halekas, J. S., & Frey, H. V. (2013). Time history of the Martian dynamo from crater magnetic field analysis. *Journal of Geophysical Research: Planets*, 118, 1488–1511. <https://doi.org/10.1002/jgre.20105>
- Mayhew, M. A. (1979). Inversion of satellite magnetic anomaly data. *Geophysical Journal International*, 45, 119–128.
- Milbury, C., Schubert, G., Raymond, C. A., Smrekar, S. E., & Langlais, B. (2012). The history of Mars’ dynamo revealed by modeling magnetic anomalies near Tyrrhenus Mons and Syrtis Major. *Journal of Geophysical Research*, 117, E10007. <https://doi.org/10.1029/2012JE004099>
- Morschhauser, A., Lesur, V., & Grott, M. (2014). A spherical harmonic model of the lithospheric magnetic field of Mars. *Journal of Geophysical Research: Planets*, 119, 1162–1188. <https://doi.org/10.1002/2013JE004555>
- Oliveira, J. S., & Wieczorek, M. A. (2017). Testing the axial dipole hypothesis for the Moon by modeling the direction of crustal magnetization. *Journal of Geophysical Research: Planets*, 122, 383–399. <https://doi.org/10.1002/2016JE005199>
- Parker, R. L. (1991). A theory of ideal bodies for seamount magnetism. *Journal of Geophysical Research*, 96(B10), 16,101–16,112.
- Plattner, A., & Simons, F. J. (2015). High-resolution local magnetic field models for the Martian south pole from Mars Global Surveyor data. *Journal of Geophysical Research: Planets*, 120, 1543–1566. <https://doi.org/10.1002/2015JE004869>
- Purucker, M., Ravat, D., Frey, H., Voorhies, C., Sabaka, T., & Acuña, M. (2000). An altitude-normalized magnetic map of Mars and its interpretation. *Geophysical Research Letters*, 27(16), 2449–2452. <https://doi.org/10.1029/2000GL000072>
- Quesnel, Y., Langlais, B., & Sotin, C. (2007). Local inversion of magnetic anomalies: Implication for Mars’ crustal evolution. *Planetary and Space Science*, 55, 258–269.
- Richmond, N. C., & Hood, L. L. (2003). Paleomagnetic pole positions of Mars. In *Lunar and Planetary Science Conference XXXIV*, Abstract 1721.
- Smith, E. J., Davis, L., Coleman, P. J. Jr., & Jones, D. E. (1965). Magnetic field measurements near Mars. *Science*, 149, 1241–1242.
- Stanley, S., Elkins-Tanton, L., Zuber, M. T., & Parmentier, E. M. (2008). Mars’ paleomagnetic field as the result of a single-hemisphere dynamo. *Science*, 321, 1822–1825.
- Telford, W. M., Geldart, L. P., & Sheriff, R. E. (1990). *Applied Geophysics* (2nd ed., pp. 62–75). Cambridge, UK: Cambridge University Press.

- Tsunakawa, H., Takahashi, F., Shimizu, H., Shibuya, H., & Matsushima, M. (2015). Surface vector mapping of the magnetic anomalies over the Moon using Kaguya and Lunar Prospector observations. *Journal of Geophysical Research: Planets*, 120, 1160–1185. <https://doi.org/10.1002/2014JE004785>
- Vervelidou, F., Lesur, V., Grott, M., Morschhauser, A., & Lillis, R. J. (2017). Constraining the date of the Martian dynamo shutdown by means of crater magnetization signatures. *Journal of Geophysical Research: Planets*, 122, 2294–2311. <https://doi.org/10.1002/2017JE005410>
- Vervelidou, F., Lesur, V., Morschhauser, A., Grott, M., & Thomas, P. (2017). On the accuracy of palaeopole estimations from magnetic field measurements. *Geophysical Journal International*, 211, 1669–1678. <https://doi.org/10.1093/gji/ggx400>